

SiPRNet: End-to-End Learning for Single-Shot Phase Retrieval

QIULIANG YE^{1*}, LI-WEN WANG¹, AND DANIEL P.K. LUN^{1, 2*}

¹ Department of Electronic and Information Engineering, The Hong Kong Polytechnic University, Hong Kong SAR, China

² The Centre for Advances in Reliability and Safety (CAiRS), Hong Kong SAR, China

* qiu-liang.ye@connect.polyu.hk; pak.kong.lun@polyu.edu.hk

Abstract: Traditional optimization algorithms have been developed to deal with the phase retrieval problem. However, multiple measurements with different random or non-random masks are needed for giving a satisfactory performance. This brings a burden to the implementation of the algorithms in practical systems. Even worse, expensive optical devices are required to implement the optical masks. Recently, deep learning, especially convolutional neural networks (CNN), has played important roles in various image reconstruction tasks. However, traditional CNN structure fails to reconstruct the original images from their Fourier measurements because of tremendous domain discrepancy. In this paper, we design a novel CNN structure, named *SiPRNet*, to recover a signal from a single Fourier intensity measurement. To effectively utilize the spectral information of the measurements, we propose a new Multi-Layer Perception block embedded with the dropout layer to extract the global representations. Two Up-sampling and Reconstruction blocks with self-attention are utilized to recover the signals from the extracted features. Extensive evaluations of the proposed model are performed using different testing datasets on both simulation and optical experimentation platforms. The results demonstrate that the proposed approach consistently outperforms other CNN-based and traditional optimization-based methods in single-shot maskless phase retrieval. The source codes of the proposed method have been released on Github: <https://github.com/Qiustander/SiPRNet>.

© 2022 Optica Publishing Group under the terms of the [Optica Publishing Group Publishing Agreement](#)

1. Introduction

Phase retrieval aims to reconstruct a complex-valued signal from its intensity-only measurements. It is a crucial problem in crystallography, optical imaging, astronomy, X-ray, electronic imaging, etc., because most existing measurement systems can only detect the relative low-frequency magnitude information of the wave fields. The study of the phase retrieval problems originated in the 1970s. The researchers of the optics community developed many reconstruction algorithms [1–3].

Mathematically, the phase retrieval problem can be described by the following equation:

$$\text{Find } \mathbf{x} \in \mathbb{C}^N \quad \text{s.t.} \quad \mathbf{y}_i = |\mathcal{F}(\mathbf{I}_i \circ \mathbf{x})|^2, i = 1, \dots, M, \quad (1)$$

where $\mathbf{x} \in \mathbb{C}^N$ is the complex-valued signal of interest, and \mathbf{y} is its Fourier intensity measurements; \circ and \mathcal{F} refer to elementwise multiplication and Fourier transform operator, respectively. The pre-defined optical masks \mathbf{I} provide the constraints to reduce the ill-posedness of the problem. It is implemented in many different ways. For instance, early-stage phase retrieval algorithms treat the support of the signal as the optical mask [2]. Specifically, $|\mathbf{x}_i| \neq 0$ when $i \in \mathcal{S}$, where \mathcal{S} denotes the support of the signal. However, these early-stage algorithms cannot guarantee the convergence of the optimization process nor provide globally optimal solutions. Recently, pre-defined random optical masks have been used as the constraints to improve the reconstruction performance [4–7]. The random masks can be implemented using a spatial light modulator (SLM) or digital micromirror device (DMD) [5, 8]. Although the usage of the random masks can

lead to better reconstruction performance, there are several disadvantages. The cost of DMD and SLM is one concern, the error due to the global gray-scale phase mismatch and spatial non-uniformity from the devices is another. Besides, it was empirically shown that about 4 – 6 measurements are required for exact recovery with random binary masks [6, 9]. It increases the measurement time and can affect the quality of the reconstructed image, particularly for dynamic objects.

Recently, data-driven methods, like deep neural networks, have been widely applied to explore the data distributions through extensive training samples [10]. Among them, the so-called Convolutional Neural Network (CNN) that exploits the features based on convolution kernels has been successfully adopted in image processing tasks, like image restoration [11–13]. Besides, an important technique named attention mechanism that mimics cognitive attention became popular in the CNN structure to enhance some parts of the feature maps and thus improve the performance [14]. Since CNN can learn discriminative representations from large training datasets, researchers have spent effort in using CNN for solving phase retrieval problems [15–18]. For instance, Chen et al. reconstructed signals from Fresnel diffraction patterns with CNN and the contrast transfer function [19]. Kumar et al. proposed the deep unrolling networks that solved the iterative phase retrieval problem with CNN [20]. Besides, the conditional generative adversarial network (GAN), a kind of data-driven generative method based on specific conditions [21], was adopted for reconstructing the phase information from Fourier intensity measurements [22]. Wu et al. also proposed a CNN to reconstruct the crystal structures with coherent X-ray diffraction patterns [23, 24]. The above methods adopt supervised learning that trains the networks with the paired ground-truth data. In recent years, training with unpaired or unsupervised (no ground-truth data) datasets has been a popular topic. For example, Fus et al. proposed the unsupervised learning for in-line holography phase retrieval [25], while Zhang et al. developed the GAN-based phase retrieval with unpaired datasets [26]. While the above approaches have achieved some success, phase retrieval with Fraunhofer diffraction patterns (i.e., Fourier intensity) for general applications is still a challenge. It is partly because of the large domain discrepancy between the Fourier plane and image plane; the large variation in data distributions of general applications also introduces much difficulty in designing a model structure that is optimal for different applications. In this paper, we propose a single-shot maskless phase retrieval method named *SiPRNet* that is benefited from the advanced deep learning technology. Compared with the traditional algorithms that need multiple intensity measurements, the proposed method only collects one Fourier intensity measurement for reconstruction. Besides, no optical mask is needed in the proposed method; thus, the cost for expensive SLM/DMD devices is saved. The proposed *SiPRNet* is designed to work with general image datasets without assuming a specific application domain. It has demonstrated its generality by achieving state-of-the-art performance on three different datasets, as shown in our experimental results. It significantly outperforms the existing optimization-based and learning-based phase retrieval methods.

The contributions of our method are: (1) We propose a novel CNN structure - *SiPRNet* that utilizes advanced deep learning techniques for single-shot maskless phase retrieval. It can reliably reconstruct the original signal based on only one Fourier intensity measurement without using optical masks. (2) We propose a Multi-Layer Perception (MLP) block to extract global representations from the intensity measurement. In addition, we propose to embed a dropout layer into the MLP block to constrain the behavior of the fully connected layers, which promotes the MLP to extract global representation. (3) We propose to use residual learning and self-attention mechanism in the Up-sampling and Reconstruction blocks, which improves the quality of the reconstructed signals. (4) We verify the proposed method on an optical platform to demonstrate its practicality. The source codes of the proposed method have been released on Github: <https://github.com/Qiustander/SiPRNet>.

The rest of this paper is organized as follows. Section 2 introduces the defocused phase

retrieval system we developed in this study and the proposed end-to-end deep-learning phase retrieval network *SiPRNet*. Section 3 presents the model analysis and simulation results. Section 4 provides the experimental results on an optical system for validating the performance of the proposed method.

2. Proposed Method

2.1. Phase Retrieval System

As indicated in Eq. (1), a phase retrieval system aims to reconstruct a complex-valued signal \mathbf{x} from its Fourier intensity measurements. The proposed method does not require multiple measurements or optical masks, so $M = 1$ and all the values of the mask \mathbf{I} are equal to one in Eq. (1). In this case, the original complex-valued signal \mathbf{x} is reconstructed only from its Fourier intensity. This seemingly impossible task is known to have a solution, although with ambiguities. From [27], it is known that \mathbf{x} can be uniquely defined, except for trivial ambiguities, by its Fourier intensity, with an oversampling factor over 2 in each dimension, if \mathbf{x} has a finite support and is non-symmetric. The above has an important implication to the optical system required for the proposed phase retrieval method. Fig. 1 shows the system we have constructed to implement the proposed method. In the system, we increase the resolution of the CMOS camera to make sure that the captured Fourier intensity image has a sampling rate at least two times in each dimension higher than that of the object image \mathbf{x} . As a result, the number of samples in the zero diffraction order of the Fourier intensity image is 762×762 , while the number of samples of \mathbf{x} is 128×128 . We then extract the central 128×128 pixels of the Fourier intensity measurements for feeding to the proposed CNN model for phase retrieval.

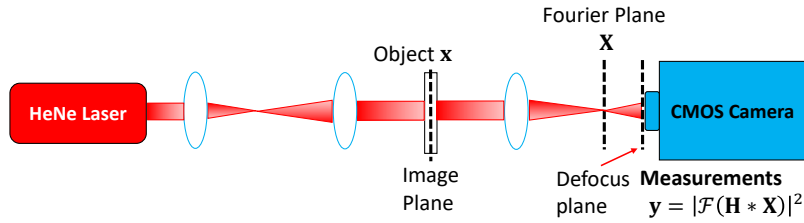


Fig. 1. Optical path of the defocus phase retrieval system. \mathbf{x} represents the complex-valued object, and \mathbf{y} is its Fourier intensity measurement; $\mathbf{X} = \mathcal{F}(\mathbf{I}_i \circ \mathbf{x})$, \mathbf{H} and $*$ denote the Fourier plane in complex-valued form, the defocus function generated via Fresnel diffraction and the convolution operation, respectively.

When capturing Fourier intensity images, it is common to have the saturation problem. It is because most structured signals have the energy concentrated in the low-frequency areas, in particular the zero frequency. Due to the limited analog-to-digital resolution of standard scientific cameras (14 - 16 bits), the central regions of the Fourier intensity measurement are often seriously saturated. To lessen the effect of the saturation problem, we convolve the Fourier intensity measurement with a defocus function \mathbf{H} to reduce the dynamic range [28]. It can be implemented by moving the camera beyond the Fourier plane. Fig. 1 shows a typical optical path for implementing the defocus phase retrieval system. Fig. 9 shows some examples of the Fourier intensity measurements obtained in our experiments.

Besides the lens-based system that we have implemented in this work, we can also find lensless phase retrieval systems [18]. Different from the lens-based system that reconstructs images from their Fraunhofer diffraction patterns, the lensless system reconstructs images based on their Fresnel diffraction patterns [18]. Compared with the lens-based system, the lensless system requires a much longer distance between the sensors and objects. For instance, in [18], the

distance between the sensor and object is reported as 37.5cm or longer. It would lead to severe aberrations and energy loss. By using a lens, the lens-based system can generate high-quality Fraunhofer diffraction patterns at a short propagation distance between the lens and sensor (3cm or less), thus avoiding the drawbacks stated above.

2.2. Deep Learning Model: SiPRNet

With the oversampling constraint as mentioned above, it is possible to reconstruct a complex-valued signal (with trivial ambiguities) from only its Fourier intensity without other constraints (such as optical masks). However, such a reconstruction problem is highly non-convex that is difficult to solve with traditional optimization methods. Due to their non-linear characteristic, deep neural networks have been successfully applied to many non-convex optimization problems. In this paper, we propose to regard the single-shot maskless phase retrieval challenge as an end-to-end learning task, and formulate the retrieval process directly by a deep neural network model (denoted as $P(\mathbf{y}; \theta)$) as:

$$\hat{\mathbf{x}} = P(\mathbf{y}; \theta), \quad (2)$$

where θ represents the learnable parameters of the deep learning model. The training target is to minimize the error between the predicted $P(\mathbf{y}; \theta)$ and the ground-truth complex-valued image \mathbf{x} regularized with the total variation (TV) norm $TV(\hat{\mathbf{x}})$. The training process can be written as:

$$P(\mathbf{y}; \theta) = \underset{\hat{\mathbf{x}}}{\operatorname{argmin}} (\|\mathbf{x} - \hat{\mathbf{x}}\|_1 + \lambda TV(\hat{\mathbf{x}})), \quad (3)$$

where $\|\cdot\|_1$ denotes the ℓ_1 -norm distance and λ is a constant determined empirically.

Fig. 2 shows the overall structure of the proposed phase retrieval network: *SiPRNet*. It mainly consists of two parts: feature extraction and phase reconstruction. It takes the Fourier intensity measurement \mathbf{y} as input and reconstructs the complex-valued image \mathbf{x} as its output.

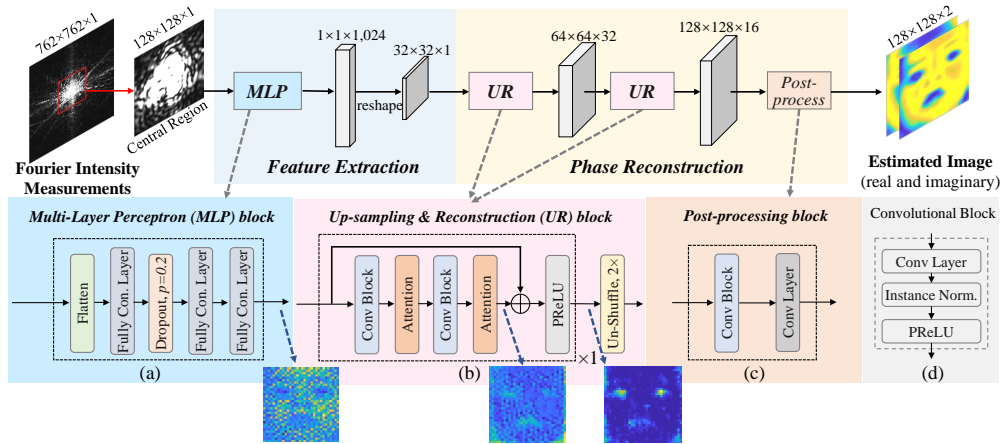


Fig. 2. Structure of the proposed network that mainly consists of two parts: Feature Extraction and Phase Reconstruction.

2.2.1. Feature Extraction

Traditional learning-based approaches often use a CNN as the front end to extract the features of the Fourier intensity measurement. However, the convolution operation of CNN shares the parameters (e.g., weights and bias) for all data of the measurement but ignores their different

characteristics. Therefore, we propose to use a new Multi-Layer Perceptron (MLP) block to fuse the information of different frequency data as shown in Fig. 2(a). The MLP block consists of three Fully Connected (FC) and one Dropout layer. The input Fourier measurement is firstly reshaped from the size of $128 \times 128 \times 1$ to $1 \times 1 \times 16,384$, and then fed to the first FC layer of the MLP block. Each FC layer has 1,024 neurons for extracting the features required for reconstructing the original complex-valued images. We propose to embed a Dropout layer after the first FC layer. The Dropout layer randomly deactivates a small number (empirically 20%) of neurons at the training stage. At the inference stage, all neurons are activated that forms an ensemble to reduce the risk of overfitting [29]. Our design with embedding a Dropout layer after the first FC layer constrains the behavior of the FC layers so that the features extracted by the MLP block do not depend on a particular input frequency measurement. The effectiveness of the dropout layer has been evaluated and shown in Section 3.2. Fig. 2 shows an example of the original complex-valued image (real and imaginary), the Fourier intensity measurement, and the features extracted by the MLP block. It can be seen that the MLP block has performed the domain conversion. The extracted feature image contains the features of the original complex-valued image. A decoder is needed to reconstruct the real and imaginary images from the extracted features.

2.2.2. Phase Reconstruction

The phase reconstruction part contains two Up-sampling and Reconstruction (UR) blocks and one Post-processing block, as shown in Fig. 2(b) and (c). The UR block is responsible for reconstructing the complex-valued image from the extracted features and progressively upsampling it back to the original size. The basic processing unit of the UR block is the convolution block that has three components: convolutional, instance normalization, and Parametric Rectified Linear Unit (PReLU) layers. The convolutional layer contains 3×3 learnable filters that aim to implicitly approximate the nonlinear backward mapping from the extracted features to the desired complex-valued image \mathbf{x} . The instance normalization and PReLU layers are non-linear functions that increase the non-linear capacity and learning ability of the deep learning model.

A self-attention unit is followed after each convolutional block. Recently, the self-attention technique has been popularly used in image reconstruction tasks, e.g., the scattering problem [30, 31]. Traditional CNN using small convolution kernels can only extract the local correlation of an image. However, natural images are often structural that exhibit global correlation. Self-attention is an effective way to exploit the global correlation in images. The structure of the self-attention layer used in the UR block is similar to that in [30], as shown in Fig. 3. At the first stage, the input features are fed to three 1×1 convolutional layers (θ , ϕ and g). The outputs are denoted as key, query, and value, respectively, all with the same dimensions. Next, the cross-correlation matrix is computed between the key and query. It represents the dependency between any two pixels of the input features. The softmax function is then performed to normalize the correlation scores and build an attention map. Large values in the attention map denote strong correlations between the features concerned. Since the correlation is computed among all features, the attention is made not only to those with local correlations but also the global ones. The result is finally multiplied with the value to generate the self-attention feature maps. They are then added back to the original features to strengthen the features of interest. Such an attention mechanism is important to the training of the UR block. It allows the UR block to reconstruct images with correlated features. For instance, for the extracted features as shown in Fig. 2, the UR block will try to reconstruct both the left and right eyes together since they have a high correlation as indicated in the training face images in the dataset. Since the correlation of the features may change at different resolutions, another UR block is used after the first one on the features of higher resolution.

Direct stacking convolutional and attention layers would lead to the obvious performance drop

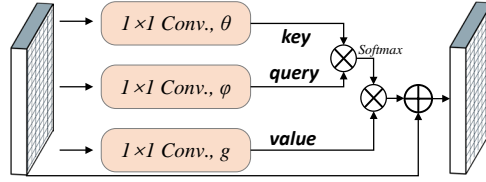


Fig. 3. Structure of the attention mechanism.

because of weak information flow and gradient vanishing [11]. Therefore, we add a shortcut connection after the convolution block and attention mechanism that forms a residual structure (shown in Fig. 2(b)), which is widely adopted in image processing tasks [32–34]. The residual setting avoids the gradient vanishing problem and therefore reduces the learning difficulty. As shown in Fig. 2, the self-attention layers effectively estimate the residue between the input feature and desired one. Finally, we utilize the unshuffle layer to reshape the feature map to enlarge the spatial sizes. The effectiveness of the residual self-attention structure is further discussed in Section 3.2.

2.2.3. Post-processing block

The Post-processing block contains two convolutional layers (shown in Fig. 2(c)). It estimates the real $\hat{\mathbf{x}}_{Re}$ and imaginary $\hat{\mathbf{x}}_{Im}$ parts of the image from the up-sampled features. Then, the phase part $\hat{\mathbf{x}}$ of the image can be calculated by:

$$\hat{\mathbf{x}} = \tan^{-1} \left(\frac{\hat{\mathbf{x}}_{Im}}{\hat{\mathbf{x}}_{Re}} \right). \quad (4)$$

2.2.4. Loss Function

We regard the phase retrieval problem as a supervised learning task. At the training stage, we prepare a set of paired training data. Each Fourier intensity measurement has a paired complex-valued image as the ground-truth target. Then, the deep learning model can be optimized by minimizing the ℓ_1 -norm distance between the estimation and the ground-truth images plus the TV-norm to improve the image edges. The loss function \mathcal{L} is defined as:

$$\mathcal{L} = \|\mathbf{x}_{Re} - \hat{\mathbf{x}}_{Re}\|_1 + \|\mathbf{x}_{Im} - \hat{\mathbf{x}}_{Im}\|_1 + \lambda TV(\hat{\mathbf{x}}). \quad (5)$$

The symbols \mathbf{x}_{Re} and \mathbf{x}_{Im} represent the ground-truth real and imaginary parts of the image, respectively.

3. Simulation Results

3.1. Simulation Setup

We conducted the simulation on two different datasets: the Real-world Affective Faces (RAF) dataset [35] and Fashion-MNIST dataset [36]. Specifically, the training data was converted to gray-scale image and resized to 128×128 . Then the pre-processed images $\mathbf{x} \in [0, 1]$ were used to generate complex-valued images of two forms: phase-only and magnitude-phase. For generating the phase-only images, we mapped \mathbf{x} to the 2π phase domain via an exponential function: $\exp(2\pi i \mathbf{x})$, with the magnitude kept as 1. On the other hand, we used the images of Fashion-MNIST dataset to generate the magnitude-phase images. To be specific, we directly used the pre-processed images $\mathbf{x} \in [0, 1]$ as the magnitudes of the images, i.e., $\mathbf{x}_{mag} = \mathbf{x} \in [0, 1]$. Then we set the phase parts through $\mathbf{x}_{phase} = \exp(2\pi i \mathbf{x}_{mag})$ and combined them by $\mathbf{x} = \mathbf{x}_{mag} \circ \mathbf{x}_{phase}$ as the magnitude-phase training and testing images, where \circ denotes the elementwise multiplication.

As mentioned in Section 2, we suggest to reduce the saturation problem by convolving the Fourier intensity measurement with a defocus function. Based on the convolution property of the Fourier transform, we can simulate it by multiplying the testing image with a defocus kernel \mathbf{h} in the spatial domain. It can be generated through the Fresnel propagation [28]. Denote the original image as $x(p, q)$ and $X(u, v)$ as its Fourier transform, then the optical field $X_L(u', v')$ in the defocus plane is expressed as:

$$X_L(u', v') = C \iint X(u, v) H(u - \frac{u'}{\lambda L}, v - \frac{v'}{\lambda L}) du dv, \quad (6)$$

where λ , L and H denotes the wavelength, distance between the lens after the object and the defocus plane, and the Fourier transform of the defocus kernel \mathbf{h} , respectively. C is the constant and $h(p, q)$ is given as $e^{\frac{j\pi}{\lambda L}c(p^2+q^2)}$. Based on the convolution theorem, Eq. (6) is equivalent to the elementwise multiplication between h and x in the spatial domain with the scaling factor λL .

Then, oversampled discrete Fourier transform (DFT) with size 762×762 (the same size as in real experiments) was performed to generate the intensity measurements. For each image, the Fourier intensity measurement was capped at the value 4095 (12-bit) to simulate the dynamic range of the practical scientific cameras. The central 128×128 patch was cropped as the input of the *SiPRNet* (the performance of different input sizes is discussed in Section 3.2.1). The total epoch and mini-batch size were set as 1,000 and 32. The Adam optimizer [37] with the learning rate of 10^{-4} was implemented to update the gradients in each training step. Note that the learning rate was updated through *StepLR* scheduler in PyTorch every 100 epoches with $\gamma = 0.9$.

We adopted Peak Signal to Noise Ratio (PSNR, higher the better), Structural Similarity (SSIM, higher the better) and Mean Absolute Error (MAE, lower the better) as the performance metrics to measure the difference between the reconstructed images $\hat{\mathbf{x}}$ and ground truth images \mathbf{x} . For each dataset, we selected the first 1,000 images in the test set as the testing samples for evaluation. We converted the reconstructed real and imaginary parts to phase-only images via Eq. (4). The phase values of both images were shifted by π to ensure non-negative values for the computation of PSNR. The average PSNR, SSIM and MAE were acquired among all 1,000 testing images for evaluation.

3.2. Ablation Study

To gain a deeper insight into the improvements obtained by *SiPRNet*, we conducted additional ablation studies on different components of our framework and analyzed their impact on the speed and accuracy of the network.

3.2.1. Impact of Input Size

For the two-dimensional Fourier spectrum, the central regions represent the low-frequency information while outer areas contain the high-frequency components. Structured signals (e.g., natural images) usually have their energy concentrated in the low-frequency regions; hence the high-frequency components have relatively lower intensity and are dominated by noise. An ablation analysis was performed to determine the size of the central regions to be used. In our experiments, the intensity measurements have the size of 762×762 . We fed the central $[32 \times 32, 64 \times 64, 128 \times 128, 256 \times 256, 512 \times 512]$ of the intensity measurement to the same network and study the performance, as shown in Fig. 4. The average testing PSNR from 30000th to 35000th training steps was chosen for comparison. The box-plot of the performance, the floating point operations per second (FLOPs) and the numbers of trainable parameters with respect to the sizes are shown in Fig. 4. Although the model performance keeps increasing along with the increase of input size, the number of the trainable parameters also boosts quickly, which brings a huge computational burden. For example, it can be seen that the number of parameters dramatically increases from 19.3M to 69.6M when the input size changes from 128×128 to

256×256 . While the growth speed of the performance is linear when the input size is smaller than 256×256 , it saturates as the input size increases to about 128×128 . Therefore, we adopt 128×128 as the input size to balance performance and efficiency.

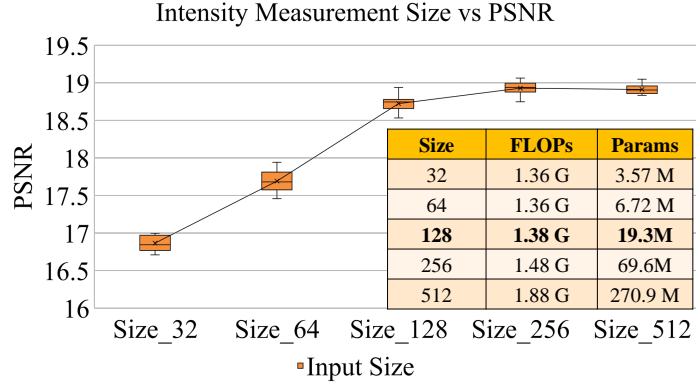


Fig. 4. Ablation study on the input sizes. The results are obtained with the RAF dataset [35].

3.2.2. Impact of Defocus Distance

The effect of the defocus distance L is discussed in this section. We investigated 6 situations of the defocus distance: $0mm$ (no defocusing), $15mm$, $20mm$, $30mm$, $45mm$, and $75mm$. The defocus kernel is a pure-phase object generated by Holoeye built-in function. The default defocus distance is $30mm$ in our proposed *SiPRNet*. The size of the input intensity measurements is 128×128 . The box-plot for average PSNR is presented in Fig. 5. As shown in the figure, the reconstruction performance significantly degrades when there is no defocusing ($L = 0mm$). It is because some pixels are severely saturated and give wrong information to the network. On the other hand, the performances are similar when $L = 15$ to $45mm$ although the PSNR is slightly higher when $L = 30mm$. It shows that the performance of the system is not sensitive to the choice of L as long as it is not too small or too big. When the defocus distance is large, i.e. $75mm$, the PSNR significantly drops. It is because a portion of the Fourier intensity measurements (high-frequency areas) become very small due to the decrease in light intensity with the long defocus distance. To balance the illumination efficiency and the reconstruction performances, the defocus distance L was selected as $30mm$ for all experiments.

3.2.3. Impact of Dropout Layer

We investigated the effect of the number of Dropout layers in feature extraction part. We set the dropout rate as 0.2 in every Dropout layer. Since 3 FC layers are used in the MLP blocks, we investigated 4 situations when introducing the Dropout layers: 0 Dropout layer, 1 Dropout layer after the first FC layer, 2 Dropout layers after each of the first two FC layers, and 3 Dropout layers after each of the FC layers. One Dropout layer is the default setting in our proposed *SiPRNet*. The size of the input intensity measurements is 128×128 . The box-plot for average PSNR is presented in Fig. 6. As shown in the figure, if there is no Dropout layer, the average PSNR of the reconstructed images is the lowest because of the over-fitting problem. The network is lazy to investigate the hidden frequency representations, and the reconstruction relies on a small number of inputs. The Dropout layer randomly deactivates a part of the inputs at the training stage, which inspires the network to find more global and robust representations. At the testing stage, all input signals are used to form an ensemble learning structure that increases the generalization power

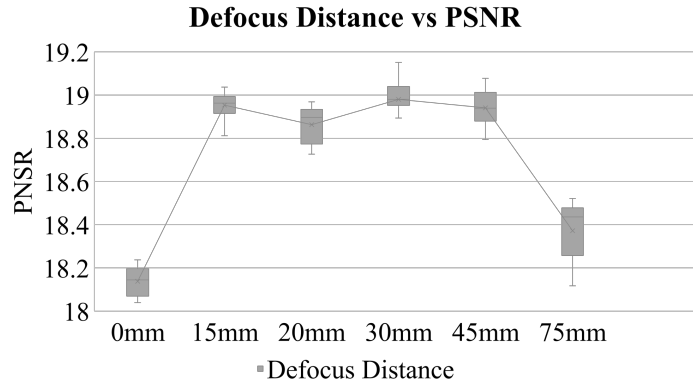


Fig. 5. Ablation study on the defocus distance. The results are obtained with the RAF dataset [35].

of the whole network. After implementing the Dropout layer, the model performance boosts as expected. Interestingly, with more dropout layers applied, there is too much information ignored in the training stage that hurts the learning progress of the network and decreases the performance. Therefore, we adopt $30mm$ as the defocus distance to balance performance and illumination efficiency.

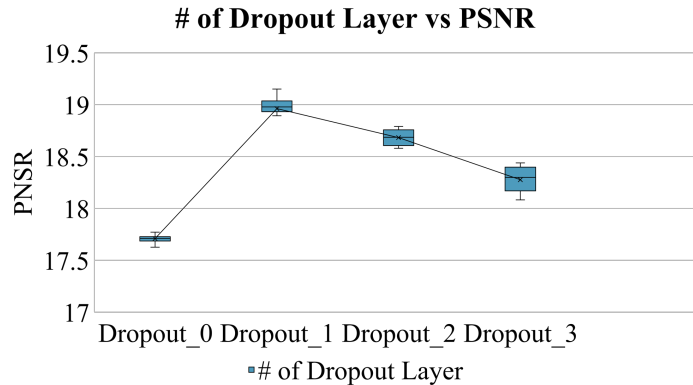


Fig. 6. Ablation study on the number of Dropout layers in feature extraction. The results are obtained with the RAF dataset [35].

3.2.4. Impact of Residual Units

We also investigated the effects of the number of residual units in the phase reconstruction part. As shown in Fig. 2, each residual unit contains two layers of Conv Blocks interlaced with two self-attention layers plus the PReLU at the end. The size of the input images to the network is still 128×128 . With everything remaining the same but just changing the number of residual units in each UR block, the average PSNRs of the estimated images are obtained and shown in Fig. 7. It can be seen that using the residual units brings in better PSNR performance. The model with one residual unit has similar or even better performance than the models with more residual units. To pursue better PSNR and efficiency, we choose to use one residual unit in the UR block.

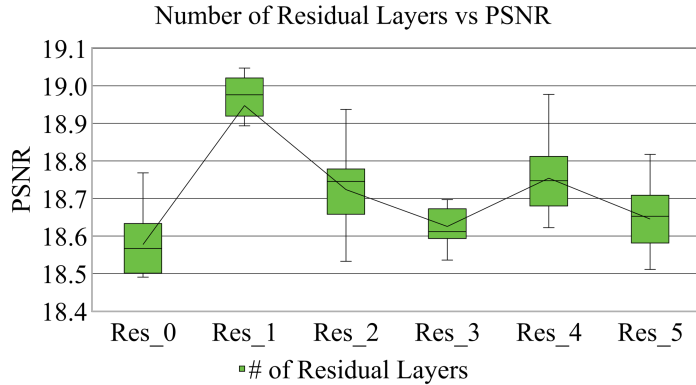


Fig. 7. Ablation study on the number of residual units. The results are obtained with the RAF dataset [35].

3.2.5. Model Robustness

Besides the generalization ability, the robustness is also a crucial metric to evaluate neural networks. The more robust the network, the less probable the overfitting problem would happen in the network. In order to demonstrate the robustness of the proposed *SiPRNet*, we utilized the K-Fold cross validation, a statistical method based on the resampling procedure [38]. The procedure of the K-Fold cross validation can be briefly described as follows: 1. Randomly shuffle the dataset. 2. Split the dataset into K groups. 3. In each fold, take a group as the testing dataset and the remaining groups as the training dataset. Then, fit the deep learning model on the training dataset and do the evaluation on the testing dataset. 4. Reset the model parameters and repeat step 3 until K folds are accomplished. 5. Summarize the model evaluation scores obtained in each fold. To be specific, we adopted $K = 5$ folds for evaluation and we ran 100 epochs in each fold. In each fold, 80% of the samples were treated as the training data and the rest 20% were utilized for testing. We used the training (for the training dataset) and testing (for the testing dataset) losses as the evaluation scores. The training loss was recorded every 20 training batches and the testing loss was collected every epoch. The simulated results on the RAF and Fashion-MNIST datasets are shown in Fig.8. As can be seen, both losses decrease quickly with the growth of the training epoch for both datasets. The curves of the losses are similar in each fold. Although there are small variations at the beginning of the training stage (5 – 15 epochs in Fig.8(a) and 10 – 25 epochs in Fig.8(b)), all folds converge to the optimal direction and thus are close to the average fold curve. In conclusion, the K-fold cross validation results demonstrate the robustness and effectiveness of *SiPRNet*.

3.3. Simulation Results

In this paper, we compare our *SiPRNet* with the traditional algorithms and learning-based methods. Compared methods include the traditional optimization-based algorithms such as Gerchberg–Saxton (GS) [1], Hybrid Input-Output (HIO) [2], and total variation ADMM (ADMM-TV) [39]. In addition, we compare the proposed *SiPRNet* with other CNN-based methods including: Plain Network (denoted as PlainNet) [11]: the basic CNN structure that stacks convolutional layers one by one; Residual Network (denoted as ResNet) [11,40]: a popular deep-learning structure and has several skip connections among the convolutional layers; residual dense network (denoted as ResDenseNet) [41]: a network that adds more skip connections to achieve better efficiency; Lensless imaging network (denoted as LenlessNet) [18]: a residual UNet to recover the phase-only images in a lensless imaging system; Conditional Generative

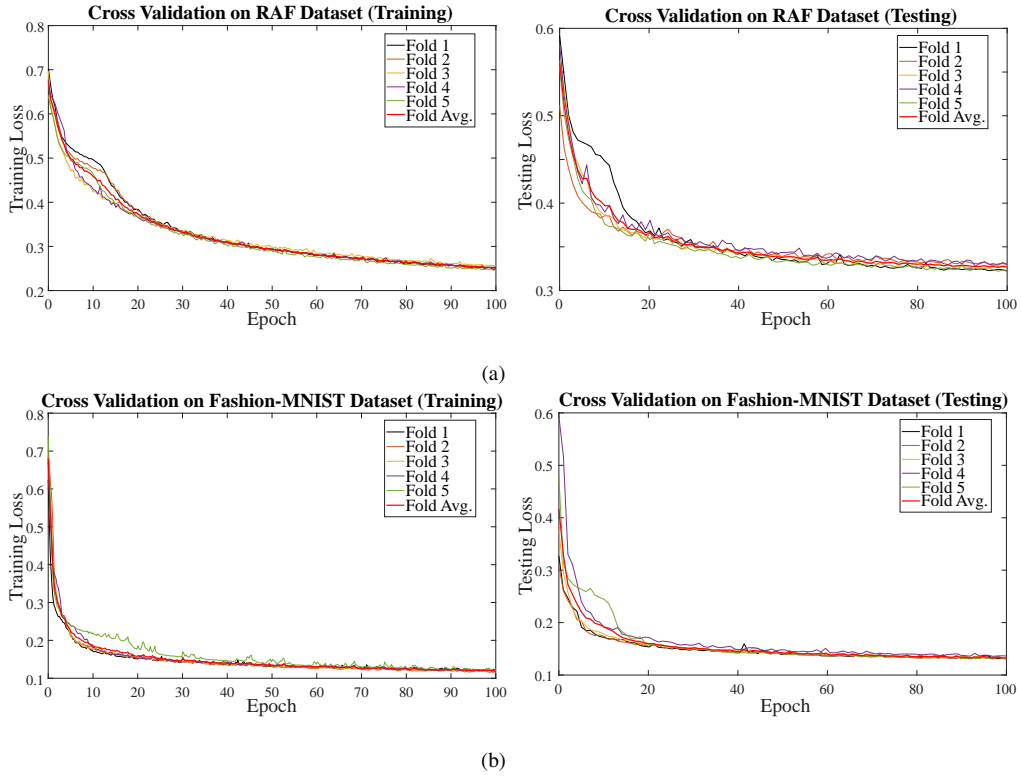


Fig. 8. Training & Testing errors of 5-Fold cross validation on (a) RAF dataset, and (b) Fashion-MNIST dataset, respectively. Fold Avg. (colored in red) denotes the mean of 5 folds.

Adversarial Phase Retrieval Network (denoted as PRCGAN) [22]: a network that utilizes the conditional adversarial learning strategy for phase retrieval task; and NNPhase [23]: a network to recover the complex-valued images from Fraunhofer diffraction patterns.

Phase-only datasets: The phase retrieval results with the phase-only datasets are shown in Table 1, Table 2, and Fig. 9. To save space, the qualitative results of PlainNet and ResDenseNet are not included in Fig. 9 due to their inferior performances. All the CNN-based methods were trained with the same settings on the RAF and Fashion-MNIST datasets. Note that the hyper-parameters of all traditional methods were optimally fine-tuned and fixed when the methods were evaluated with all testing images. For each traditional optimization-based method, we did three different trials of evaluation for each testing image, where each trial had 400 iterations. We manually selected the reconstructed image with the highest PSNR as the final result for comparison. For the CNN-based methods, we compared the average PSNR of reconstructed images given by the trained models at the last epoch.

As can be seen in Table 1 and Table 2, the proposed *SiPRNet* achieves much better performance than all compared methods. Compared with the traditional optimization-based methods, *SiPRNet* has average PSNR and SSIM gains of at least $6.544dB$ and 0.457 , respectively, on the RAF dataset (Table 1). The PSNR and SSIM gains can even reach $19.58dB$ and 0.816 , respectively, on the Fashion-MNIST dataset (Table 2). This is because traditional optimization-based methods cannot converge to satisfactory results with only one intensity measurement. As shown in Fig. 9, only ADMM-TV method can recover the contour of the facial images (7th column). In addition, *SiPRNet* can achieve PSNR and SSIM gains of at least $1.631dB$ and 0.065 , respectively, compared

with other state-of-the-art CNN-based methods on the two datasets. It can be seen in Fig. 9 that the reconstructed images of the proposed *SiPRNet* outperform other CNN-based methods qualitatively. In addition, the error maps (4th column) also show that the estimated images are close to the ground-truth images. As can be seen, the reconstructed images only differ from the original ones in some local areas with minor errors, while most regions are close to 0.

Note that we train all the networks with our quantized defocused Fraunhofer diffraction patterns datasets. Although the reconstructed images via PRCGAN [22] seem to have better high-frequency information (facial details), the reconstructed image does not share similarities with the original image (last second column). In fact, the performance of PRCGAN in our simulation is poorer than that reported in the original paper of PRCGAN. It is because the dataset used in the original simulation of PRCGAN does not consider the saturation problem, which is commonly found when imaging the Fourier intensity. Besides, the authors assume the object images are magnitude-only (no phase information), which is far from real situations. As for NNPhase [24], it aims to deal with the crystal data that the application is quite specific. Besides, LenslessNet [18] is initially designed for the phase retrieval task based on Fresnel diffraction patterns with lensless imaging systems. When testing with the more general and realistic datasets used in our simulations, the performances of these networks drop significantly compared with those reported in their original papers. We will show in the next section that these networks also suffer from the same problems in the real experiments. The above simulation results show that the proposed *SiPRNet* outperforms the traditional optimization-based and CNN-based methods both quantitatively and qualitatively. More simulation results can be found in Appendix.

We also evaluate the inference speed of different methods by collecting the mean execution time of one hundred samples. The results are presented in Table 1 (last column). Since our approach is designed in an end-to-end manner that can effectively utilize the huge computational power of the current advanced GPU devices, it can be seen in Table 1 that the proposed the *SiPRNet* is very fast and can realize real-time performance (3.569 ms/img). It is comparable with other learning-based approaches. In contrast, the inference speed of the traditional algorithms is quite slow (in the order of seconds) since lots of iterations are required, and they can only be implemented with the CPU.

Magnitude-phase dataset: The simulation results are shown in Fig. 10. We select HIO, NNPhase, and PRCGAN for comparison since they all perform Fourier phase retrieval. It can be seen that the proposed *SiPRNet* outperforms all compared approaches. In particular, the results show that PRCGAN cannot deal with the complex-valued phase retrieval tasks, and it is difficult for HIO to reconstruct complex-valued images with single-shot intensity measurement. The magnitude and phase images given by these approaches have poor quality. As is presented in Fig. 10(b), the proposed *SiPRNet* achieves much better performance than all compared methods evaluated by different metrics. For the magnitude part, the proposed *SiPRNet* achieves average PSNR and SSIM gains of at least 2.145dB and 0.156, respectively. For the phase part, the increases in PSNR and SSIM gains can reach 3.214dB and 0.181, respectively. The above simulation results show that the proposed *SiPRNet* can be generalized to complex-valued image datasets (containing both magnitude and phase parts) and outperform the existing methods.

4. Experimental Results

4.1. Experimental Setup

We also evaluated our proposed *SiPRNet* with a practical optical system. A picture of the experimental setup is shown in Fig. 11. It comprises a Thorlabs 10mW HeNe laser with wavelength $\lambda = 632.8nm$; and a 12-bit 1920 × 1200 Kiralux CMOS camera with pixel pitch 5.86 μm . Besides, the optical system includes one 75mm, three 100mm, and one 150mm lenses to form a standard imaging system. The choice of the lenses is for generating Fourier intensity images of appropriate size to match the size of the CMOS sensor. In practice, these lenses can

Table 1. Quantitative comparison (average MAE/PSNR/SSIM/Inference Time) with the state-of-the-art methods for phase retrieval on the RAF dataset. Best and second best performances are in red and blue colors, respectively.

Methods	MAE ↓		PSNR ↑		SSIM ↑		Inference Time (ms/img)
	Sim.	Exp.	Sim.	Exp.	Sim.	Exp.	
GS [1]	0.969	1.147	15.099	12.770	0.250	0.129	1.233×10^3
HIO [2]	1.007	1.185	14.854	12.554	0.239	0.127	1.226×10^3
ADMM-TV [39]	1.119	1.600	12.660	9.902	0.206	0.025	1.324×10^4
PlainNet [11]	0.975	1.180	13.841	12.479	0.425	0.377	1.583
ResNet [11, 40]	0.894	0.812	15.178	15.831	0.456	0.471	2.438
ResDenseNet [41]	1.084	1.010	13.344	13.800	0.380	0.387	1.732
LenslessNet [18]	0.671	0.704	17.573	17.132	0.598	0.596	7.396
PRCGAN [22]	0.951	0.945	14.738	14.833	0.511	0.508	0.983
NNPhase [23]	0.755	0.931	16.753	15.416	0.558	0.544	5.834
SiPRNet (Ours)	0.570	0.582	19.204	18.905	0.663	0.663	3.569

Table 2. Quantitative comparison (average MAE/PSNR/SSIM) with the state-of-the-art methods for phase retrieval on the Fashion-MNIST dataset. Best and second best performances are in red and blue colors, respectively.

Methods	MAE ↓		PSNR ↑		SSIM ↑	
	Sim.	Exp.	Sim.	Exp.	Sim.	Exp.
GS [1]	1.571	1.681	9.852	9.176	0.088	0.053
HIO [2]	1.594	1.709	9.629	9.082	0.068	0.052
ADMM-TV [39]	0.935	1.366	13.772	9.973	0.226	0.132
PlainNet [11]	0.589	0.601	16.916	16.672	0.629	0.623
ResNet [11, 40]	0.289	0.304	21.394	20.806	0.739	0.726
ResDenseNet [41]	0.381	0.419	19.406	18.252	0.675	0.657
LenslessNet [18]	0.179	0.221	26.784	23.833	0.842	0.802
PRCGAN [22]	1.598	1.602	10.102	10.126	0.422	0.417
NNPhase [23]	0.404	0.426	23.956	22.778	0.739	0.443
SiPRNet (Ours)	0.127	0.144	29.209	28.132	0.884	0.872

be compactly arranged such that the whole imaging system can be made very small. However, the lens design is out of the scope of this study. A 1920×1080 Holoeye Pluto phase-only SLM with pixel pitch $\delta_{SLM} = 8\mu m$ was used to generate the testing objects in the experiments. Specifically, the images in the two datasets mentioned above were loaded to the SLM to impose multiple-level phase changes. The images were pre-multiplied with a defocus kernel; thus, there was no need to move the camera beyond the focal plane. It is to ensure that the defocusing process, which is not our main focus, will be perfectly implemented so that we only need to focus on the reconstruction performances of different methods. The defocus kernel is a pure-phase object generated by Holoeye built-in function corresponding to $L = 30mm$. The reason for choosing

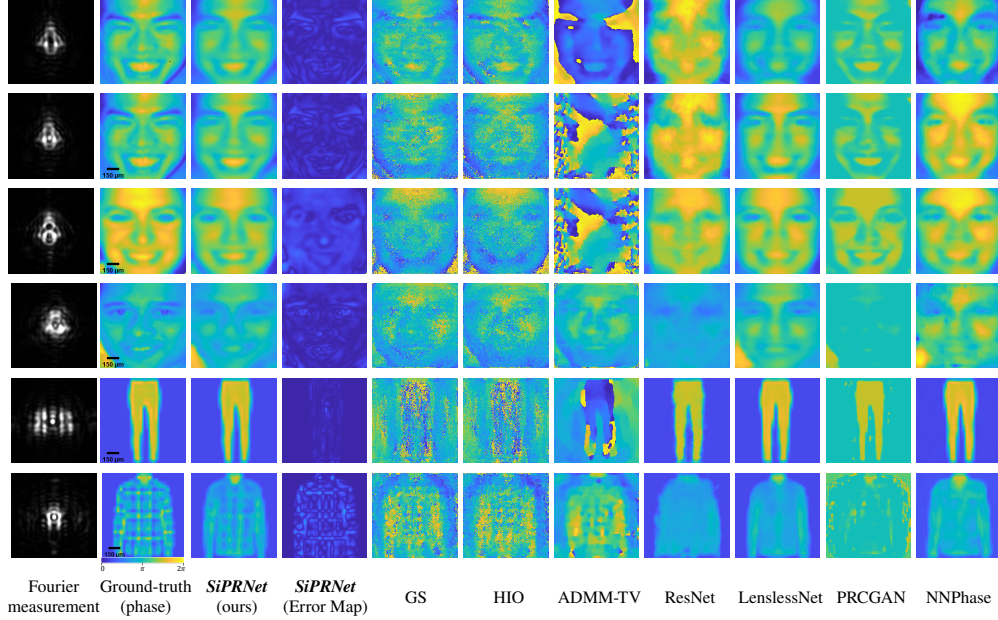


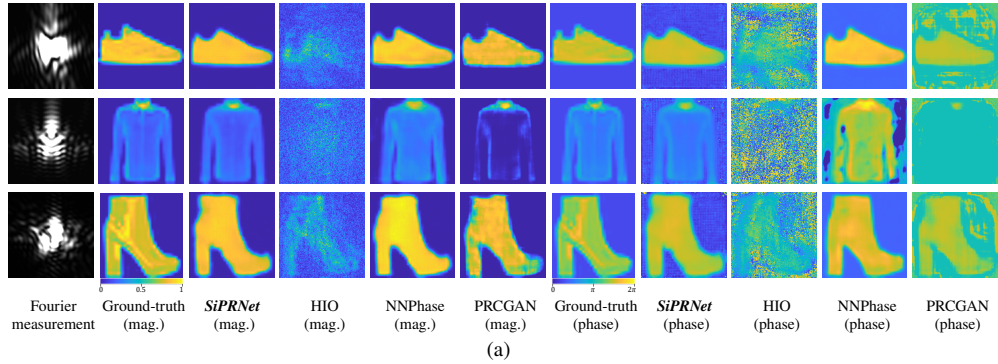
Fig. 9. Simulation and experimental results of different phase retrieval methods on the RAF [35] and the Fashion-MNIST datasets [36]. The first **column** denotes the Fourier intensity measurements (pixel values: $0 \rightarrow 4095$). The second **column** shows the corresponding phase parts of the complex-valued images with scale bars (for experimental results) at the bottom left corners. The fourth **column** denotes the error maps of *SiPRNet*. The other **columns** present the reconstructed images through different methods. Except for the Fourier intensity measurements (the first **column**), the colormap of the rest **columns** ranges from 0 to 2π . The first and second **rows** are the simulation and experimental results of the same image from the RAF dataset. The third and the fourth **rows** show the experimental performances of other images in the RAF dataset. The fifth and the sixth **rows** indicate the experimental results of images from the Fashion-MNIST dataset. Please zoom in for better view. More results can be found in Appendix.

$L = 30mm$ has been explained in Section 3.2.2. We utilized the central 128×128 SLM pixels in all experiments. The resulting Fourier intensity measurements were captured by the camera and formed the training and testing datasets for *SiPRNet*. The size of the acquired measurement is $\frac{\lambda L}{d}$ where d denotes the pixel pitch of the SLM.

4.2. Experimental Results

With the training dataset, we fine-tuned all the pre-trained models acquired in the simulation with the experimental measurements. That is, we re-trained the models with the trained parameters from the simulation and used the experimental measurements as the new training inputs. The quantitative and qualitative experimental results are presented in Table 1, Table 2, and Fig. 9, respectively.

It is clearly shown in Table 1 and Table 2 that the experimental results of *SiPRNet* only decline a little compared with the simulation results. It proves the robustness of the proposed method. As shown in Fig. 9, all traditional optimization-based methods fail to reconstruct the original images because it is insufficient to converge to satisfactory solutions with only one intensity measurement for those methods. Compared with other state-of-the-art CNN-based methods,



Methods	MAE ↓		PSNR ↑		SSIM ↑	
	Mag.	Phase	Mag.	Phase	Mag.	Phase
HIO [2]	0.298	1.898	7.709	8.317	0.330	0.043
PRCGAN [22]	0.073	1.654	18.672	9.924	0.588	0.387
NNPhase [23]	0.109	0.687	18.169	18.752	0.395	0.46
SiPRNet (Ours)	0.053	0.359	20.817	21.966	0.744	0.594

(b)

Fig. 10. (a) Qualitative simulation results of different phase retrieval methods on the magnitude-phase Fashion-MNIST datasets [36]. The pixel values of the Fourier intensity measurements (first column) range from 0 to 4095. The colormap of the magnitude parts (second to the sixth columns) ranges from 0 to 1, while the colormap of the phase parts (seventh to the last columns) ranges from 0 to 2π . Please zoom in for better view. (b) Quantitative comparisons (average MAE/PSNR/SSIM) on the same dataset. Best performances are denoted in **bold** font.

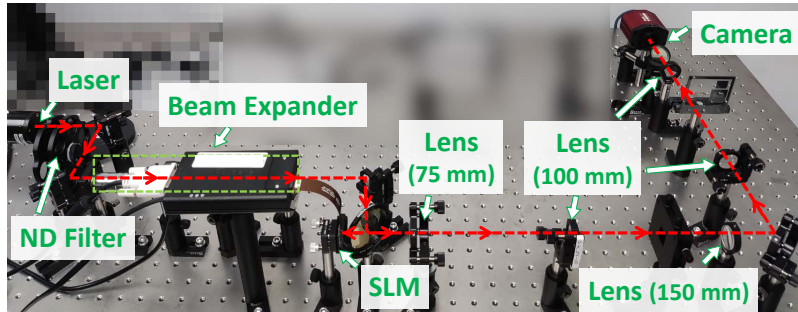


Fig. 11. Experimental setup of the defocus phase retrieval system.

SiPRNet can achieve at least $1.773dB$ and 0.067 gains in PSNR and SSIM, respectively, on the two datasets. As can be clearly seen in Fig. 9, the proposed *SiPRNet* can reconstruct the most similar contours as the ground truth and preserve more high-frequency details compared with other methods. The above experimental results show that the proposed *SiPRNet* outperforms all traditional optimization-based and CNN-based methods quantitatively and qualitatively when using in practical phase retrieval systems. However, there is always room for improvement. It is shown in the results of all learning-based approaches that the reconstructed images are a bit blurry compared with the ground truths. We note that for the captured intensity images, the values of the

high-frequency components are much smaller than those in the low-frequency areas. The noise in the images further makes the high-frequency components difficult to identify. It introduces much difficulty to the neural networks to extract the features of the high-frequency components. Further investigation is needed to improve the sharpness of the reconstructed images. Extra denoising and attention modules may be applied to better recover the high-frequency components.

5. Conclusion

In conclusion, this paper proposed an end-to-end CNN structure for single-shot maskless phase retrieval. We have shown how the optical system should be constructed to ensure the feasibility of the solution and reduce the saturation problem due to the high dynamic range of Fourier intensity measurements. We proposed a novel CNN named *SiPRNet* to reconstruct phase-only images with the central areas of the intensity measurements. To fully extract the representative features, we proposed an MLP block embedded with a Dropout layer to fuse the information of the frequency components. A self-attention structure was included to enhance the global correlation in the reconstructed phase images. The simulation and experimental results demonstrate that the proposed *SiPRNet* performs much better than the traditional phase retrieval algorithms and other CNN structures, making it a promising solution to practical phase retrieval applications. At the moment, we only conduct simulations and experiments on synthesized objects. Further research is underway to enhance the network structure for working with more complex image datasets and realistic objects.

Appendix

In this Appendix, we show additional qualitative comparison results. Fig. 12, 13, 14 present the simulation and experimental results. The detailed explanations are attached with each figure.

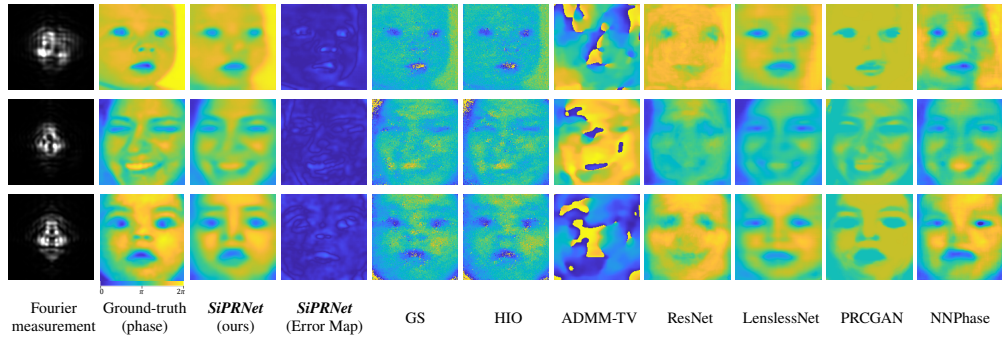


Fig. 12. Simulation results of different phase retrieval methods on the RAF dataset [35]. The first **column** denotes the Fourier intensity measurements (pixel values: $0 \rightarrow 4095$). The second **column** shows the corresponding phase parts of the complex-valued images. The fourth **column** denotes the error maps of the *SiPRNet*. The other **columns** present the reconstructed images through different methods. Except for the Fourier intensity measurements (the first **column**), the colormap of the rest **columns** ranges from 0 to 2π . Each **row** presents the simulation results of a testing image. Please zoom in for better view.

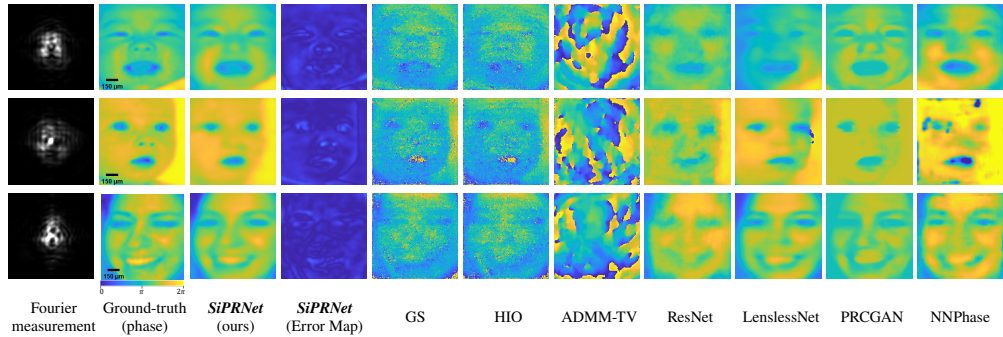


Fig. 13. Experimental results of different phase retrieval methods on the RAF dataset [35]. The first **column** denotes the Fourier intensity measurements (pixel values: $0 \rightarrow 4095$). The second **column** shows the corresponding phase parts of the complex-valued images with scale bars at the bottom left corners. The fourth **column** denotes the error maps of *SiPRNet*. The other **columns** present the reconstructed images through different methods. Except for the Fourier intensity measurements (the first **column**), the colormap of the rest **columns** ranges from 0 to 2π . Each **row** presents the experimental results of a testing image. Please zoom in for better view.

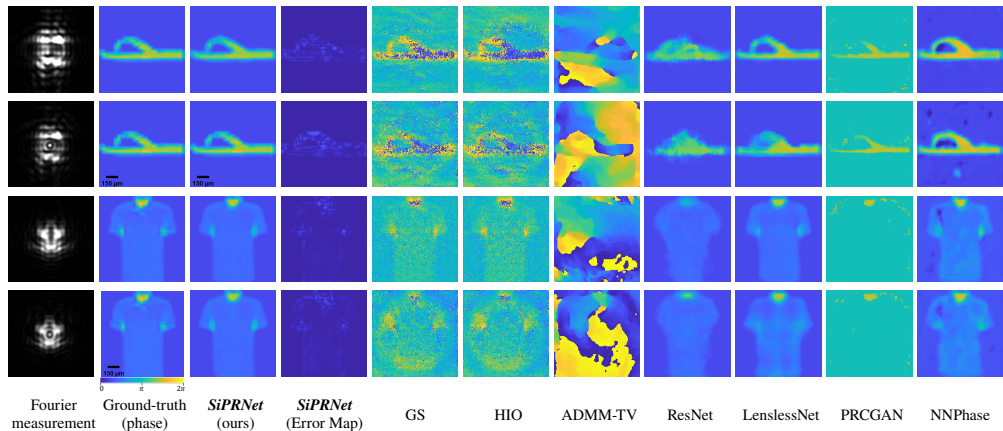


Fig. 14. Simulation and experimental results of different phase retrieval methods on the Fashion-MNIST dataset [36]. The first **column** denotes the Fourier intensity measurements (pixel values: $0 \rightarrow 4095$). The second **column** shows the corresponding phase parts of the complex-valued images with scale bars (for experimental results) at the bottom left corners. The fourth **column** denotes the error maps of *SiPRNet*. The other **columns** present the reconstruction images through different methods. Except for the Fourier intensity measurements (the first **column**), the colormap of the rest **columns** ranges from 0 to 2π . The first and second **rows** present the simulation and experimental results of the same image. The third and the fourth **rows** show the simulation and experimental results of another image. Please zoom in for better view.

Data availability

The datasets used in this paper are available in [35, 36]. Data underlying the results presented in this paper are not publicly available at this time but may be obtained from the authors upon reasonable request.

Funding

General Research Fund (PolyU 15225321), Centre for Advances in Reliability and Safety (CAiRS)

Acknowledgments

This work was supported by the Hong Kong Research Grant Council under General Research Fund no. PolyU 15225321, and the Centre for Advances in Reliability and Safety (CAiRS) admitted under AIR@InnoHK Research Cluster.

Disclosures

The authors declare no conflicts of interest.

References

1. R. W. Gerchberg, "A practical algorithm for the determination of phase from image and diffraction plane pictures," *Optik* **35**, 237–246 (1972).
2. J. R. Fienup, "Phase retrieval algorithms: a comparison," *Appl. Opt.* **21**, 2758–2769 (1982).
3. J. M. Rodenburg, "Ptychography and related diffractive imaging methods," *Adv. Imaging Electron Phys.* **150**, 87–184 (2008).
4. A. Anand, G. Pedrini, W. Osten, and P. Almero, "Wavefront sensing with random amplitude mask and phase retrieval," *Opt. Lett.* **32**, 1584–1586 (2007).
5. R. Horisaki, Y. Ogura, M. Aino, and J. Tanida, "Single-shot phase imaging with a coded aperture," *Opt. letters* **39** **22**, 6466–9 (2014).
6. E. J. Candes, X. Li, and M. Soltanolkotabi, "Phase retrieval via wirtinger flow: Theory and algorithms," *IEEE Transactions on Inf. Theory* **61**, 1985–2007 (2015).
7. Q. Ye, Y.-H. Chan, M. G. Somekh, and D. P. Lun, "Robust phase retrieval with green noise binary masks," *Opt. Lasers Eng.* **149**, 106808 (2022).
8. C. Zheng, R. Zhou, C. Kuang, G. Zhao, Z. Yaqoob, and P. So, "Digital micromirror device-based common-path quantitative phase imaging," *Opt. Lett.* **42** **7**, 1448–1451 (2017).
9. E. J. Candes, X. Li, and M. Soltanolkotabi, "Phase retrieval from coded diffraction patterns," *Appl. Comput. Harmon. Analysis* **39**, 277–299 (2015).
10. Y. LeCun, Y. Bengio, and G. Hinton, "Deep learning," *Nature* **521**, 436–444 (2015).
11. K. He, X. Zhang, S. Ren, and J. Sun, "Deep residual learning for image recognition," in *Proceedings of the IEEE Conference on Computer Vision and Pattern Recognition (CVPR)*, (2016).
12. K. Zhang, W. Zuo, Y. Chen, D. Meng, and L. Zhang, "Beyond a gaussian denoiser: Residual learning of deep cnn for image denoising," *IEEE transactions on image processing* **26**, 3142–3155 (2017).
13. L.-W. Wang, Z.-S. Liu, W.-C. Siu, and D. P. Lun, "Lightening network for low-light image enhancement," *IEEE Transactions on Image Process.* **29**, 7984–7996 (2020).
14. A. Vaswani, N. Shazeer, N. Parmar, J. Uszkoreit, L. Jones, A. N. Gomez, L. u. Kaiser, and I. Polosukhin, "Attention is all you need," in *Advances in Neural Information Processing Systems*, vol. 30 I. Guyon, U. V. Luxburg, S. Bengio, H. Wallach, R. Fergus, S. Vishwanathan, and R. Garnett, eds. (Curran Associates, Inc., 2017).
15. M. Deng, S. Li, A. Goy, I. Kang, and G. Barbastathis, "Learning to synthesize: robust phase retrieval at low photon counts," *Light. Sci. & Appl.* **9** (2020).
16. J. White and Z. Chang, "Attosecond streaking phase retrieval with neural network," *Opt. Express* **27**, 4799–4807 (2019).
17. J. Shi, X. Zhu, H. Wang, L. Song, and Q. Guo, "Label enhanced and patch based deep learning for phase retrieval from single frame fringe pattern in fringe projection 3d measurement," *Opt. Express* **27**, 28929–28943 (2019).
18. A. Sinha, J. Lee, S. Li, and G. Barbastathis, "Lensless computational imaging through deep learning," *Optica* **4**, 1117–1125 (2017).
19. C. Bai, M. Zhou, J. Min, S. Dang, X. Yu, P. Zhang, T. Peng, and B. Yao, "Robust contrast-transfer-function phase retrieval via flexible deep learning networks," *Opt. Lett.* **44**, 5141–5144 (2019).
20. S. Kumar, "Phase retrieval with physics informed zero-shot network," *Opt. Lett.* **46**, 5942–5945 (2021).
21. M. Mirza and S. Osindero, "Conditional generative adversarial nets," (2014).
22. T. Uelwer, A. Oberstraß, and S. Harmeling, "Phase retrieval using conditional generative adversarial networks," in *2020 25th International Conference on Pattern Recognition (ICPR)*, (IEEE, 2021), pp. 731–738.
23. L. Wu, P. Juhas, S. Yoo, and I. Robinson, "Complex imaging of phase domains by deep neural networks," *IUCrJ.* **8**, 12–21 (2021).
24. L. Wu, S. Yoo, A. F. Suzana, T. A. Assefa, J. Diao, R. J. Harder, W. Cha, and I. K. Robinson, "Three-dimensional coherent x-ray diffraction imaging via deep convolutional neural networks," *npj Comput. Mater.* **7** (2021).
25. F. Fus, Y. Yang, A. Pacureanu, S. Bohic, and P. Cloetens, "Unsupervised solution for in-line holography phase retrieval using bayesian inference," *Opt. Express* **26**, 32847–32865 (2018).

26. Y. Zhang, M. A. Noack, P. Vagovic, K. Fezzaa, F. Garcia-Moreno, T. Ritschel, and P. Villanueva-Perez, "Phasegan: a deep-learning phase-retrieval approach for unpaired datasets," *Opt. Express* **29**, 19593–19604 (2021).
27. M. Hayes, "The reconstruction of a multidimensional sequence from the phase or magnitude of its fourier transform," *IEEE Transactions on Acoust. Speech, Signal Process.* **30**, 140–154 (1982).
28. J. Goodman, *Introduction to Fourier Optics* (W. H. Freeman, 2017).
29. N. Srivastava, G. Hinton, A. Krizhevsky, I. Sutskever, and R. Salakhutdinov, "Dropout: a simple way to prevent neural networks from overfitting," *The journal machine learning research* **15**, 1929–1958 (2014).
30. X. Wang, R. Girshick, A. Gupta, and K. He, "Non-local neural networks," in *Proceedings of the IEEE conference on computer vision and pattern recognition*, (2018), pp. 7794–7803.
31. Y. Wang, Z. Lin, H. Wang, C. Hu, H. Yang, and M. Gu, "High-generalization deep sparse pattern reconstruction: feature extraction of speckles using self-attention armed convolutional neural networks," *Opt. Express* **29**, 35702–35711 (2021).
32. F. Wang, M. Jiang, C. Qian, S. Yang, C. Li, H. Zhang, X. Wang, and X. Tang, "Residual attention network for image classification," in *Proceedings of the IEEE Conference on Computer Vision and Pattern Recognition (CVPR)*, (2017).
33. X. Zhang, L. Han, W. Zhu, L. Sun, and D. Zhang, "An explainable 3d residual self-attention deep neural network for joint atrophy localization and alzheimer's disease diagnosis using structural mri," *IEEE journal biomedical health informatics* (2021).
34. K. Park, J. W. Soh, and N. I. Cho, "Dynamic residual self-attention network for lightweight single image super-resolution," *IEEE Transactions on Multimed.* (2021).
35. S. Li, W. Deng, and J. Du, "Reliable crowdsourcing and deep locality-preserving learning for expression recognition in the wild," in *2017 IEEE Conference on Computer Vision and Pattern Recognition (CVPR)*, (IEEE, 2017), pp. 2584–2593.
36. H. Xiao, K. Rasul, and R. Vollgraf, "Fashion-mnist: a novel image dataset for benchmarking machine learning algorithms," (2017).
37. D. P. Kingma and J. Ba, "Adam: A method for stochastic optimization," (2017).
38. M. Stone, "Cross-validatory choice and assessment of statistical predictions," *J. Royal Stat. Soc. Ser. B (Methodological)* **36**, 111–133 (1974).
39. H. Chang, Y. Lou, Y. Duan, and S. Marchesini, "Total variation-based phase retrieval for poisson noise removal," *SIAM J. on Imaging Sci.* **11**, 24–55 (2018).
40. Y. Nishizaki, R. Horisaki, K. Kitaguchi, M. Saito, and J. Tanida, "Analysis of non-iterative phase retrieval based on machine learning," *Opt. Rev.* **27**, 136–141 (2020).
41. Y. Zhang, Y. Tian, Y. Kong, B. Zhong, and Y. Fu, "Residual dense network for image super-resolution," in *Proceedings of the IEEE Conference on Computer Vision and Pattern Recognition (CVPR)*, (2018).